



PACIFIC EARTHQUAKE ENGINEERING RESEARCH CENTER

Development of Geotechnical Capabilities in OpenSees

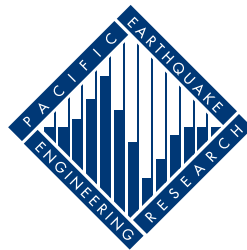
Boris Jeremic'

Department of Civil and Environmental Engineering
University of California, Davis

The Pacific Earthquake Engineering Research Center (PEER), headquartered at UC Berkeley, is a consortium of western U.S. universities working in partnership with business, industry, and government to identify and reduce the risks from major earthquakes to life safety and to the economy.

PEER achieves its objectives of earthquake risk reduction through a coordinated program of research, education, and partnerships with users of research results. PEER's research program includes basic and applied components of seismology, engineering, architecture, urban planning, and economics.

PEER is supported by grants from various public and private sources and by primary funding through the Earthquake Engineering Research Centers Program of the National Science Foundation under Award Number EEC-9701568.



PEER reports are available individually or by yearly subscription from the National Information Service for Earthquake Engineering (NISEE). To order PEER Reports, contact the

Pacific Earthquake Engineering Research Center
1301 S. 46th Street
Richmond, California 94804-4698
Tel: 510-231-9403
Fax: 510-231-9461

Disclaimer

The opinions, findings, and conclusions or recommendations expressed in this publication are those of the author(s) and do not necessarily reflect the views of the study sponsor(s) or the Pacific Earthquake Engineering Research Center.

Development of Geotechnical Capabilities in OpenSees

PEER – 2132000-3

Boris Jeremić

University of California, Davis

Pacific Earthquake Engineering Research Center

University of California, Berkeley

September 2001

Abstract

The PEER OpenSees project covers research on the “Next Generation Analytical Platform for Nonlinear Dynamic Analysis.” This report presents in some detail work performed for the “Development of Geotechnical Capabilities in OpenSees,” PEER project 2132000-3 started in May 2000. This report describes:

- Development and implementation of the universal, template constitutive driver for OpenSees;
- Development of fully coupled, solid–fluid formulation;
- Development and implementation of visualization tools for solids in OpenSees;
- Examples of soil-foundation-structure interaction simulations; and
- Development of OpenSees implementation quality control tools.

Acknowledgment

The described work would not have been possible without generous support from the Pacific Earthquake Engineering Research Center through the Earthquake Engineering Research Centers Program of the National Science Foundation under Award Number EEC-9701568. The author wishes to acknowledge help and support from Professors Gregory Fenves, Ahmed Elgamal, Pedro Arduino, and Dr. Francis McKenna. The author would also like to thank his Ph.D. students Zhaohui Yang and Xiaoyan Wu for diligent work of the highest quality.

Contents

1	Introduction	1
2	Template Elastic–Plastic Computations	3
2.1	Command Examples	3
2.2	Example Simulations	5
3	Fully Coupled, Solid–Fluid Formulation and Implementation	13
3.1	Governing Equations for Fully Saturated Behavior with a Single Pore Fluid	13
3.2	General Mixed Numerical Solution	14
3.3	Fully Coupled Analysis of Soils in Large Deformation Realm	17
4	Visualization	19
4.1	Visualizations Using Fantom	19
4.2	Visualizations Using Joey3D	21
5	Examples of Soil–Foundation–Structure Interaction Simulations	23
5.1	Static Pushover Tests	23
5.2	Humboldt Bay Bridge Retrofit	27
6	Implementation Quality Control	29

List of Figures

2.1	Monotonic triaxial loading on soil sample modeled using Drucker-Prager yield surface, Drucker-Prager flow direction, and perfectly plastic hardening rule.	5
2.2	Cyclic triaxial loading on soil sample modeled using Drucker-Prager yield surface, Drucker-Prager flow direction, and perfectly plastic hardening rule.	6
2.3	Cyclic loading results for Drucker-Prager yield surface, von Mises flow direction, and nonlinear tensorial (rotational kinematic) hardening rule. . . .	7
2.4	Monotonic triaxial compression loading results for normally consolidated soil sample modeled using Drucker-Prager yield surface, Manzari-Dafalias flow direction, and bounding surface hardening rule.	7
2.5	Monotonic triaxial compression loading results for heavily overconsolidated soil sample modeled using Drucker-Prager yield surface, Manzari-Dafalias flow direction, and bounding surface hardening rule.	8
2.6	Cyclic triaxial loading results for normally consolidated soil sample modeled using Drucker-Prager yield surface, Manzari-Dafalias flow direction, and bounding surface hardening rule.	8
2.7	Monotonic triaxial compression on slightly overconsolidated soil sample using Cam-Clay yield surface, Cam-Clay flow direction, and nonlinear scalar hardening rule (Cam-Clay).	9
2.8	Monotonic triaxial compression on heavily overconsolidated soil sample using Cam-Clay yield surface, Cam-Clay flow direction, and nonlinear scalar hardening rule (Cam-Clay).	10

2.9	Cyclic triaxial loading on slightly overconsolidated soil sample using Cam–Clay yield surface, Cam–Clay flow direction, and nonlinear tensorial (rotational kinematic) hardening rule.	10
2.10	Monotonic shearing of a slightly overconsolidated soil sample using Cam–Clay yield surface, Cam–Clay flow direction, and nonlinear scalar hardening rule (Cam–Clay).	11
2.11	Cyclic shear loading on highly overconsolidated soil sample using the Cam–Clay yield surface, the Cam–Clay flow direction, and nonlinear scalar hardening rule (of Cam–Clay type).	11
4.1	Hyperstreams-surfaces for minor principal stress (compression) for (a) a single-pile and (b) a four-pile group.	20
4.2	Visualization with Joey3D: displaced piles, moment diagram (from integrated normal stresses), shear force diagram (from integrated shear stresses), and horizontal pressure (from the first derivatives of shear forces).	21
4.3	Visualization with Joey3D: normal stresses in a solid pile.	22
4.4	Plastified zones (plastic Gauss–points) during static pushover analysis of single pile. Visualization with Joey3D: (a) side view, (b) top (plan) view.	22
5.1	(a) Single pile model, dimensions and layers of sand and clay. (b) Single pile model, side view; top four finite elements are clay, middle four layers of finite elements are sand and the bottom is all clay; interface zone around the concrete pile is also present.	24
5.2	Plastic zone at the end of loading for case 1, layers of sand and clay: (a) side view, (b) top view.	24
5.3	Plastic zone at the end of loading for case 2, single layer of clay: (a) side view, (b) top view.	25
5.4	(a) Moment, shear force, and pressure distribution (clay–sand profile); (b) p-y curves (clay–sand profile).	25
5.5	(a) Moment, shear force, and pressure distribution (clay profile); (b) p-y curves (clay profile).	26

5.6	Humboldt Bay Bridge plan of the SFS system.	27
5.7	Humboldt Bay Bridge: before and after the retrofit finite element models. .	28
5.8	Synthetic accelerations used in this analysis.	28
5.9	Response for the before and after the retrofit SFS system.	28

Chapter 1

Introduction

This report presents in some detail work performed for the PEER project, “Development of Geotechnical Capabilities in OpenSees.” The project lasted from May of 2000 until October 2001. While the report cannot cover all the work performed enough details are given for the interested reader, while a list of referenced papers that gives a more detailed overview of work is provided. In particular this report describes:

- Development and implementation of the universal, template constitutive driver for OpenSees (Chapter 2);
- Development of fully coupled, solid–fluid formulation (Chapter 3);
- Development and implementation of visualization tools for solids in OpenSees (Chapter 4);
- Example soil–foundation–structure interaction simulations (Chapter 5); and
- Development of OpenSees implementation quality control tools (Chapter 6).

Chapter 2

Template Elastic–Plastic Computations

In this part of the report some details are presented of a new approach to computations in elasto–plastic geomechanics. The approach is based on object–oriented design philosophy and on observations of the similarity of most incremental elastic–plastic material models. This new approach to elastic–plastic computations in geomechanics allows for creation of template material models. The analysis of template material models will in turn allow for easy implementation of other elastic–plastic material models based on object–oriented design principles. A detailed description of the Template Elastic–Plastic Computational Tools is given by [Jeremić and Yang, 2001], (also available in pre-print at <http://sokocalo.engr.ucdavis.edu/~jeremic/publications/CGM0102.pdf>). The following presents a brief overview of some of the command examples and illustrative simulations.

2.1 Command Examples

In order to facilitate the smooth creation of new material models, an interpreter was implemented using Tool Command Language (Tcl) [Ousterhout and Tcl/Tk Consortium,]. As an example the input commands for the elastic–plastic material model created from the Drucker–Prager yield surface, the von Mises potential surface, and the linear scalar

hardening law are presented. The commands that create this model are given below:

```
set YS "-DP"  
set PS "-VM"  
set ES1 "-Leq 1.0"  
set ET1 "-Linear 0.0"  
set stressp "0.10 0 0 0 0.10 0 0 0 0.10"  
set EPS "70000.0 70000.0 0.2 1.8 -NOD 1 -NOS 2 0.2 0.0 -stressp $stressp"  
nDMaterial Template3Dep 1 -YS $YS -PS $PS -EPS $EPS -ELS1 $ES1 -ELT1 $ET1
```

The first four lines are used to set up the elastic–plastic material model:

1. Yield Surface using Drucker–Prager function `set YS "-DP"`.
2. Plastic flow directions using von Mises potential surface `set PS "-VM"`.
3. Scalar evolution law (hardening and/or softening) `set ES1 "-Leq 1.0"`. This particular command describes the single scalar evolution law evolving with equivalent strain, using number 1.0 as a coefficient.
4. Tensorial evolution law `set ET1 "-Linear 0.0"`. In this particular case there is one tensorial hardening variable using plastic deviatoric strain but the coefficient is specified as 0.0, so it does not affect the solution.

The fifth line is used to set up the initial stress at a given material point. In this particular case, `set stressp "0.10 0 0 0 0.10 0 0 0 0.10"`, the initial stress state, is set to the isotropic stress $\sigma_{xx} = \sigma_{yy} = \sigma_{zz} = 0.10$. The sixth line is used to set up the elastic–plastic state. In this case the initial and the current modulus of elasticity $E_0 = 70000.0$, $E = 70000.0$ are set. The initial modulus of elasticity E_0 is the one at reference pressure (100kPa), and E is the current one. One can supply $E = 0.0$, for it is computed (by default) according to the current pressure using the Non–linear Elastic Model #1 described by [Jeremić and Yang, 2001]. The Poisson’s ratio is also set as $\nu = 0.2$ as well as the mass density $\rho = 1.8$. After that, the number of tensorial internal variables (`-NOD 1`) and the number of scalar internal variables as well as their initial values (`-NOS`

2 0.2 0.0) are set. Here the friction angle ϕ is specified in terms of $\alpha = 2 \sin \phi / (\sqrt{3}(3 - \sin \phi))$, which in this case is defined as $\alpha = 0.2$ and a cohesion, defined as $c = 0.0$. Lastly, that same command line provides the initial stress state for the elasto–plastic state (`-stressp $stressp`). The last command line `nDMaterial Template3Dep 1 ...` is used to combine all the ingredients into a new elastic–plastic material model which is labeled *1*.

2.2 Example Simulations

In this section a number of representative numerical simulations are presented. The main goal is to show how different yield criteria, flow directions, and hardening/softening rules can be combined to create elastic–plastic material models.

One of the simplest models to be tried first is obtained by combining the Drucker–Prager yield surface, the Drucker–Prager flow directions, and the perfectly plastic hardening rule. Figure 2.1 shows the results from a monotonic triaxial loading on one such sample. As expected the load–displacement response is bilinear. The volumetric response is at first compressive (within the elastic limits) and then becomes dilative when the material becomes elastic–plastic.

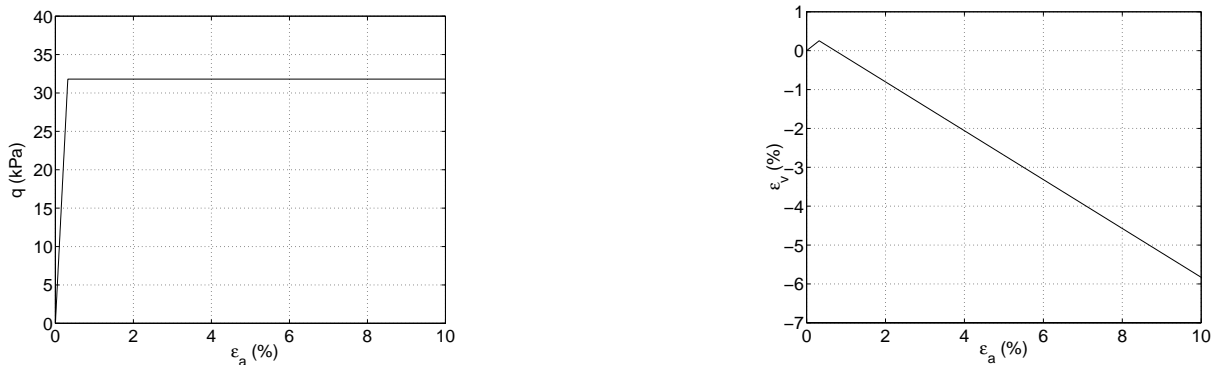


Figure 2.1: Monotonic triaxial loading on soil sample modeled using Drucker-Prager yield surface, Drucker-Prager flow direction, and perfectly plastic hardening rule.

Figure 2.2 shows results for cyclic loading of a triaxial sample using the same simple

material model described above. The load–displacement curve follows a simple closed loop. Volumetric response is compressive (elastic portion) and then becomes dilative upon yielding of the elastic–plastic material. The compressive response is recovered during unloading but the volumetric response is dilative in general.

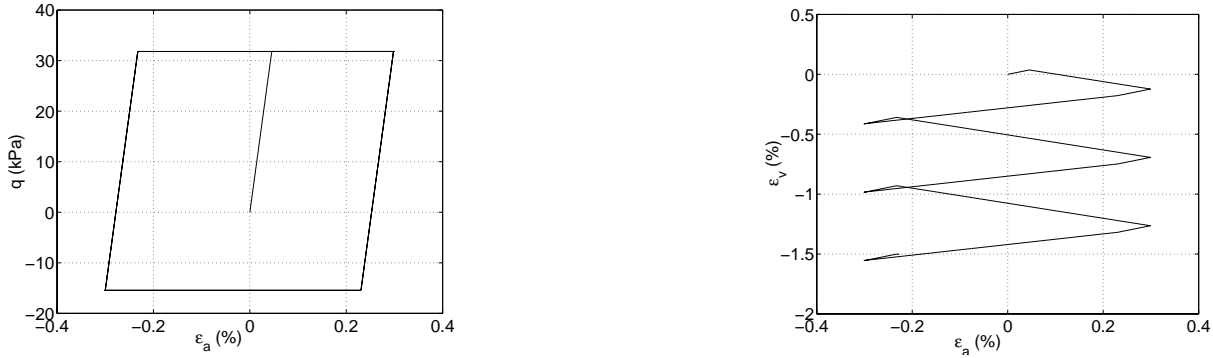


Figure 2.2: Cyclic triaxial loading on soil sample modeled using Drucker-Prager yield surface, Drucker-Prager flow direction, and perfectly plastic hardening rule.

Figure 2.3 shows the results for cyclic loading of a triaxial one–element setup using the Drucker-Prager yield surface, the von Mises flow direction, and the nonlinear tensorial hardening rule. The load–displacement curve shows a sizable elastic region, particularly for larger confinement stress. Volumetric response is mostly compressive. It should be noted that the initial plastic flow directions are deviatoric (initial plastic potential is von Mises surface). During the loading–unloading–reloading cycles the von Mises plastic potential surface will rotate (since rotational kinematic hardening was used) and thus create significant plastic volumetric strains. Those volumetric strains can be easily followed in $\epsilon_v - \epsilon_a$ diagram of Figure 2.3.

The results presented above show the behavior of elastic–plastic materials obtained by combining different yield surfaces, plastic flow directions (potential surfaces), and hardening rules.

A more realistic response for soils can be obtained by combining the above elements of an elastic–plastic model with other, more sophisticated elements. For example, an excellent material model for sand can be obtained by combining the Drucker-Prager yield

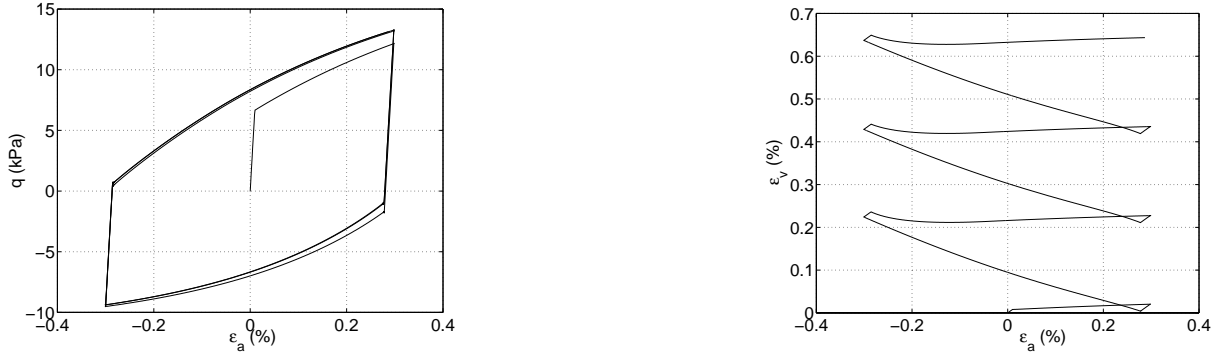


Figure 2.3: Cyclic loading results for Drucker-Prager yield surface, von Mises flow direction, and nonlinear tensorial (rotational kinematic) hardening rule.

surface, the Manzari-Dafalias flow direction, and the bounding surface hardening rule [Manzari and Dafalias, 1997].

Figure 2.4 shows the results for a monotonic loading of a triaxial one-element setup using Drucker-Prager yield surface, the Manzari-Dafalias flow direction, and the bounding surface hardening rule. The material model parameters used are taken from a paper by Manzari and Dafalias, 1997, and represent a normally consolidated sand specimen.

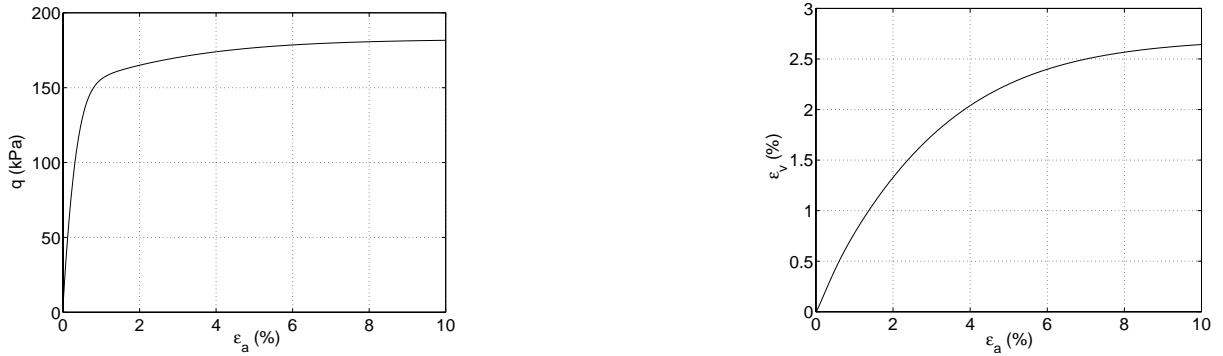


Figure 2.4: Monotonic triaxial compression loading results for normally consolidated soil sample modeled using Drucker-Prager yield surface, Manzari-Dafalias flow direction, and bounding surface hardening rule.

Figure 2.5 shows the results for the highly overconsolidated sand specimen using a similar elastic-plastic material model, namely the Drucker-Prager yield surface, the Manzari-

Dafalias flow direction, and the bounding surface hardening rule. Both the hardening and then softening load–displacement responses are observed. The volumetric response is initially compressive and then the specimen dilates.

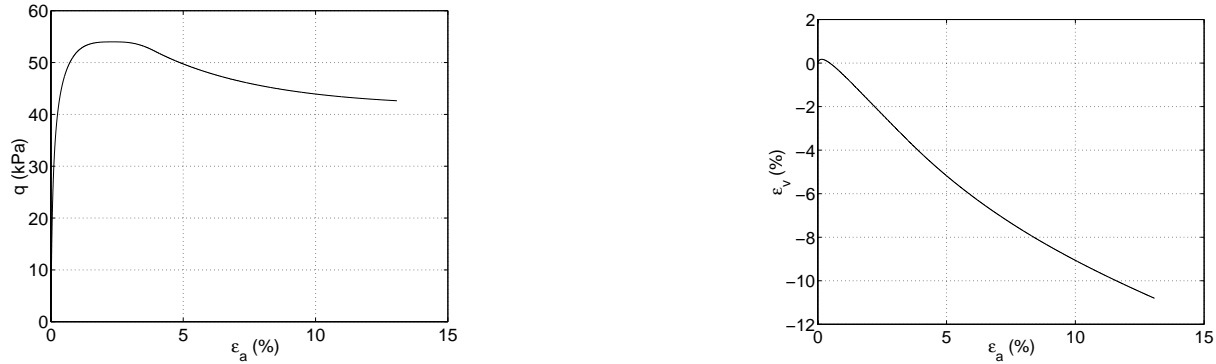


Figure 2.5: Monotonic triaxial compression loading results for heavily overconsolidated soil sample modeled using Drucker-Prager yield surface, Manzari-Dafalias flow direction, and bounding surface hardening rule.

Figure 2.6 shows the results for cyclic triaxial loading of a normally consolidated sand specimen using the same elastic–plastic material model as above. The load–displacement curve shows near saturation after a few cycles, while the volumetric response is compressive.

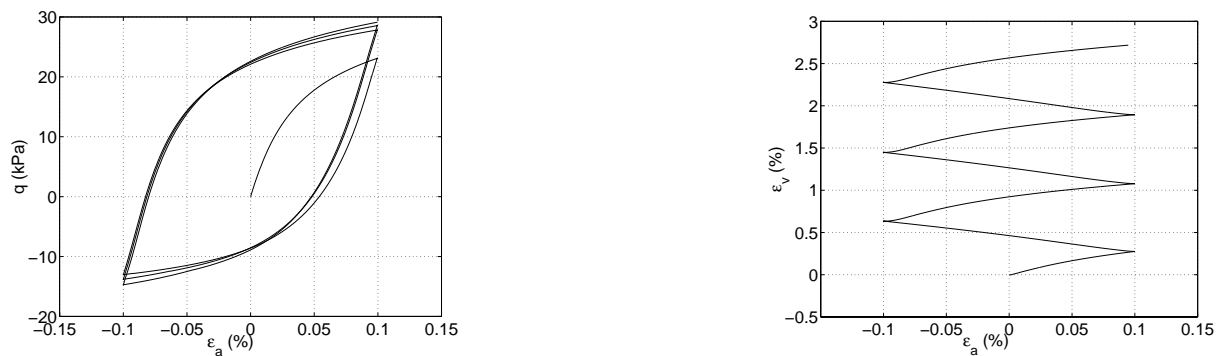


Figure 2.6: Cyclic triaxial loading results for normally consolidated soil sample modeled using Drucker-Prager yield surface, Manzari-Dafalias flow direction, bounding surface hardening rule.

One of the most widely used elastic–plastic material models is the modified Cam–Clay material model. Figures 2.7 – 2.9 show the results for the triaxial, one–element setup using the Cam–Clay yield surface, the Cam–Clay potential surface and nonlinear scalar hardening rule (Cam–Clay). In particular, Figure 2.7 shows the results for a slightly overconsolidated specimen. The load–displacement response is initially linear and then elastic–plastic, while the volumetric response is compressive. Figure 2.8 shows the re-

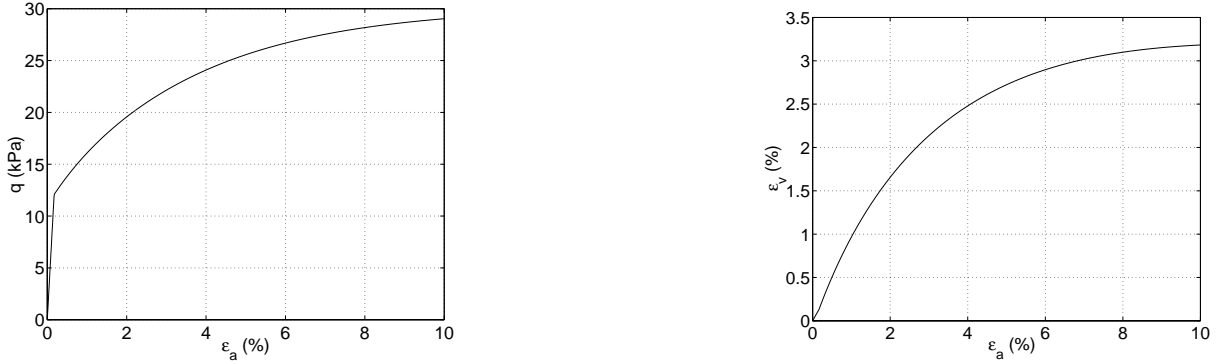


Figure 2.7: Monotonic triaxial compression on slightly overconsolidated soil sample using Cam–Clay yield surface, Cam–Clay flow direction, and nonlinear scalar hardening rule (Cam–Clay).

sponse for the same material parameters as above except that the specimen is heavily overconsolidated. Initial load–displacement response is elastic, while after yielding, the response curve softens toward the critical state. The volumetric response is initially compressive, while after yielding it becomes dilative. Figure 2.9 shows the response for a cyclic loading of a triaxial, one–element setup using the Cam–Clay yield surface, the Cam–Clay flow direction, and the nonlinear tensorial (rotational kinematic) hardening rule.

Figure 2.10 shows a monotonic shearing test for a slightly overconsolidated soil specimen. The elastic–plastic material model used was represented by a combination of Cam–Clay yield and potential surfaces, and a nonlinear scalar hardening rule. Figure 2.11 shows the results for a cyclic shear test using a material model similar to that above. The only difference is that the the soil sample is now highly overconsolidated. It is interesting to note that the sharp failure point, expected for the highly overconsolidated specimen

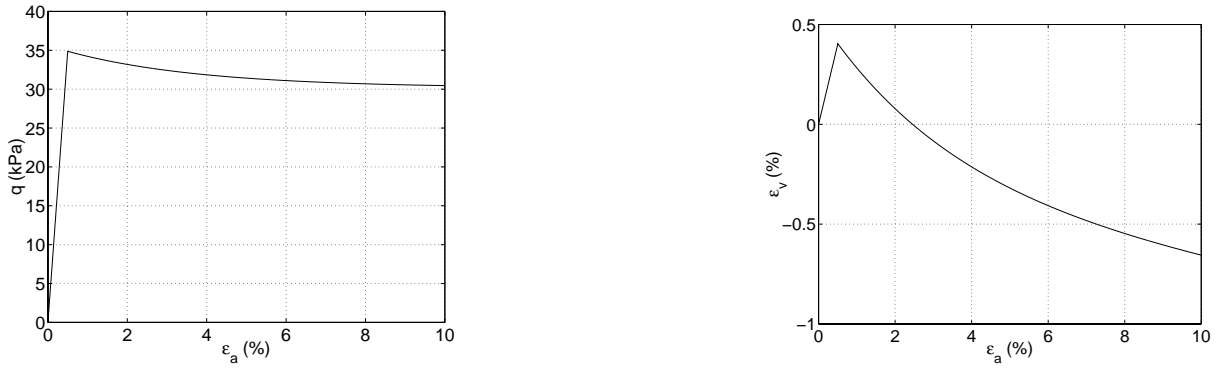


Figure 2.8: Monotonic triaxial compression on heavily overconsolidated soil sample using Cam–Clay yield surface, Cam–Clay flow direction, and nonlinear scalar hardening rule (Cam–Clay).

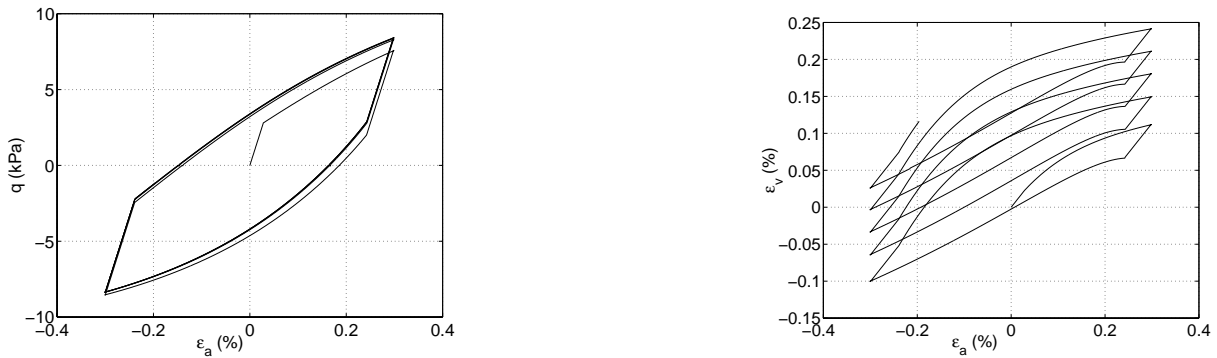


Figure 2.9: Cyclic triaxial loading on slightly overconsolidated soil sample using Cam–Clay yield surface, Cam–Clay flow direction, and nonlinear tensorial (rotational kinematic) hardening rule.

modeled using the Cam–Clay model (compare with Figure 2.8), is missing. The explanation is that the state of stress in the one element shear model is not uniform and some Gauss–points fail before others, thus smoothing the response curves.

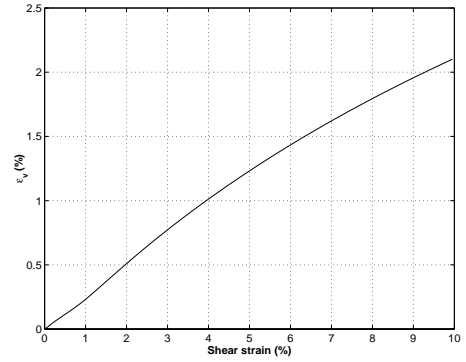
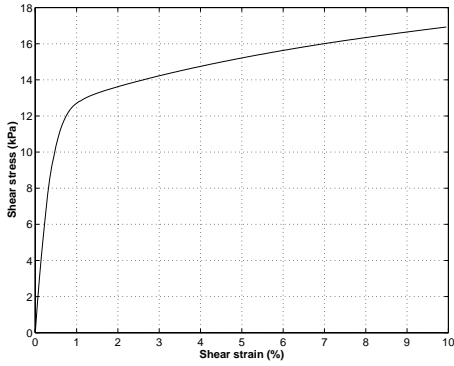


Figure 2.10: Monotonic shearing of a slightly overconsolidated soil sample using Cam–Clay yield surface, Cam–Clay flow direction, and nonlinear scalar hardening rule (Cam–Clay).

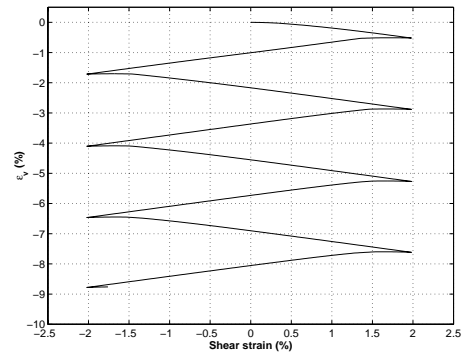
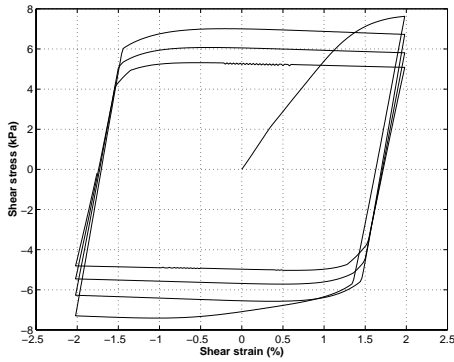


Figure 2.11: Cyclic shear loading on highly overconsolidated soil sample using the Cam–Clay yield surface, the Cam–Clay flow direction, and nonlinear scalar hardening rule (of Cam–Clay type).

Chapter 3

Fully Coupled, Solid–Fluid

Formulation and Implementation

In this section a brief description is given of the formulation and implementation of the fully coupled, solid fluid solid finite elements. Their implementation into OpenSees is currently under way (as of mid–September 2001) and first test runs are expected by early October 2001.

3.1 Governing Equations for Fully Saturated Behavior with a Single Pore Fluid

The formulations described below follow earlier work [Zienkiewicz and Shiomi, 1984]. Although the formulation may seem overly detailed (a lot of equations), they are used as reference for implementation. The **nDarray** tool [Jeremić and Sture, 1998] is used for implementing the equations below directly into OpenSees.

The effective stress principle is formulated as

$$\sigma'_{ij} = \sigma_{ij} + \delta_{ij}p \quad (3.1)$$

Constitutive relations are written in incremental format as

$$d\sigma'_{ij} = E_{ijkl} (d\varepsilon_{kl} - d\varepsilon_{kl}^0) \quad (3.2)$$

The strain increments of the soil matrix can be determined in terms of displacement increments du_i as (small strain assumption)

$$d\varepsilon_{ij} = \frac{1}{2}(du_{i,j} + du_{j,i}) \quad (3.3)$$

The overall equilibrium or momentum balance relation for the soil-fluid “mixture” can be then written as

$$\sigma_{ij,j} - \rho\ddot{u}_i - \rho_f[\underline{\dot{w}_i + \dot{w}_j\dot{w}_{i,j}}] + \rho b_i = 0 \quad (3.4)$$

where b_i is the body force acceleration. The underlined term refers to the acceleration of the fluid, written in Eulerian terms and including the relative convective term.

The second equilibrium equation ensures the momentum balance of the fluid, written as

$$-p_{,i} - \frac{R_i}{n} - \rho_f\ddot{u}_i - \underline{\rho_f[\ddot{w}_i + \dot{w}_j\dot{w}_{i,j}]/n} + \rho_f b_i = 0 \quad (3.5)$$

in which R_i represents the viscous drag forces which, assuming the Darcy seepage law, can be written as

$$\frac{R_i}{n} = k_{ij}^{-1}w_j \quad \text{or} = k^{-1}w_i \quad (3.6)$$

where k_{ij} represents non-isotropic Darcy permeability coefficients.

The flow conservation equation is written as

$$w_{i,i} + \alpha\varepsilon_{ii} + \frac{\dot{p}}{Q} + n\underline{\frac{\dot{\rho}_f}{\rho_f}} + \dot{s}_0 = 0 \quad (3.7)$$

where

$$\frac{1}{Q} \equiv \frac{n}{K_f} + \frac{\alpha - n}{K_s} \cong \frac{n}{K_f} + \frac{1 - n}{K_s} \quad (3.8)$$

3.2 General Mixed Numerical Solution

A Modification of Variables is introduced. In place of the relative displacements of the fluid w_i the total displacement of the fluid U_i is

$$U_i = u_i + \frac{w_i}{n} \quad (3.9)$$

Then the equation of the solid skeleton equilibrium becomes

$$\sigma'_{ij,j} - (\alpha - n)p_{,i} + (1 - n)\rho_s b_i - (1 - n)\rho_s \ddot{u}_i + R_i = 0 \quad (3.10)$$

The second equation will simply be $[n \times (3.5)]$, i.e.,

$$-np_{,i} - R_i - n\rho_f(\ddot{u}_i + \frac{\ddot{w}_i}{n}) + \underline{\rho_f \dot{w}_j \dot{w}_{i,j}} + n\rho_f b_i = 0 \quad (3.11)$$

By noticing $\ddot{U}_i = \ddot{u}_i + \ddot{w}_i/n$ and neglecting the $\dot{w}_j \dot{w}_{i,j}$ term,

$$-np_{,i} + n\rho_f b_i - n\rho_f \ddot{U}_i - R_i = 0 \quad (3.12)$$

The main unknowns u_i , U_i , and p can be approximated by using shape functions as

$$\begin{aligned} u_i &= N_K^u \bar{u}_{Ki} \\ U_i &= N_K^U \bar{U}_{Ki} \\ p &= N_K^p \bar{p}_K \end{aligned} \quad (3.13)$$

After some algebraic computations the system of discretized equations reads

$$\begin{bmatrix} \mathbf{M}_s & 0 & 0 \\ 0 & 0 & 0 \\ 0 & 0 & \mathbf{M}_f \end{bmatrix} \begin{bmatrix} \ddot{\bar{u}} \\ \ddot{\bar{p}} \\ \ddot{\bar{U}} \end{bmatrix} + \begin{bmatrix} \mathbf{C}_1 & 0 & -\mathbf{C}_2 \\ 0 & 0 & 0 \\ -\mathbf{C}_2^T & 0 & \mathbf{C}_3 \end{bmatrix} \begin{bmatrix} \dot{\bar{u}} \\ \dot{\bar{p}} \\ \dot{\bar{U}} \end{bmatrix} + \begin{bmatrix} \mathbf{K}^{EP} & -\mathbf{G}_1 & 0 \\ \mathbf{G}_1^T & \mathbf{P} & \mathbf{G}_2^T \\ 0 & -\mathbf{G}_2 & 0 \end{bmatrix} \begin{bmatrix} \bar{u} \\ \bar{p} \\ \bar{U} \end{bmatrix} = \begin{bmatrix} \bar{f}_s \\ \bar{f}_p \\ \bar{f}_f \end{bmatrix} \quad (3.14)$$

or

$$\begin{aligned} &\begin{bmatrix} (M_s)_{KijL} & 0 & 0 \\ 0 & 0 & 0 \\ 0 & 0 & (M_f)_{KijL} \end{bmatrix} \begin{bmatrix} \ddot{u}_{Lj} \\ \ddot{p}_L \\ \ddot{U}_{Lj} \end{bmatrix} + \begin{bmatrix} (C_1)_{KijL} & 0 & -(C_2)_{KijL} \\ 0 & 0 & 0 \\ -(C_2)_{LjiK} & 0 & (C_3)_{KijL} \end{bmatrix} \begin{bmatrix} \dot{u}_{Lj} \\ \dot{p}_L \\ \dot{U}_{Lj} \end{bmatrix} \\ &+ \begin{bmatrix} (K^{EP})_{KijL} & -(G_1)_{KiL} & 0 \\ (G_1)_{LjK} & (P)_{KL} & (G_2)_{LjK} \\ 0 & -(G_2)_{KiL} & 0 \end{bmatrix} \begin{bmatrix} \bar{u}_{Lj} \\ \bar{p}_L \\ \bar{U}_{Lj} \end{bmatrix} = \begin{bmatrix} (\bar{f}_s)_{Ki} \\ (\bar{f}_p)_K \\ (\bar{f}_f)_{Ki} \end{bmatrix} \end{aligned} \quad (3.15)$$

Or written in a familiar form as

$$\mathcal{M}\ddot{x} + \mathcal{C}\dot{x} + \mathcal{K}u = f \quad (3.16)$$

where

$$\begin{aligned}
\mathbf{M}_s &= (M_s)_{KijL} = \int_{\Omega} N_K^u (1-n) \rho_s \delta_{ij} N_L^u d\Omega \\
\mathbf{M}_f &= (M_f)_{KL} = \int_{\Omega} N_K^U n \rho_f \delta_{ij} N_L^U d\Omega \\
\mathbf{C}_1 &= (C_1)_{KijL} = \int_{\Omega} N_K^u n^2 k_{ij}^{-1} N_L^u d\Omega \\
\mathbf{C}_2 &= (C_2)_{KijL} = \int_{\Omega} N_K^u n^2 k_{ij}^{-1} N_L^U d\Omega \\
\mathbf{C}_3 &= (C_3)_{KijL} = \int_{\Omega} N_K^U n^2 k_{ij}^{-1} N_L^U d\Omega \\
\mathbf{K}^{EP} &= (K^{EP})_{KimP} = \int_{\Omega} N_{K,j}^u D_{ijml} N_{P,l}^u d\Omega \\
\mathbf{G}_1 &= (G_1)_{KiL} = \int_{\Omega} N_{K,i}^u (\alpha - n) N_L^p d\Omega \\
\mathbf{G}_2 &= (G_2)_{KiL} = \int_{\Omega} n N_{K,i}^U N_L^p d\Omega \\
\mathbf{P} &= P_{KL} = \left[\int_{\Omega} N_K^p \frac{1}{Q} N_L^p d\Omega \right] p_L \\
(\bar{f}_s)_{Ki} &= (f_1^u)_{Ki} - (f_4^u)_{Ki} + (f_5^u)_{Ki} \\
(f_f)_{Ki} &= (f_1)_{Ki} - (f_2)_{Ki} \\
(f_1^u)_{Ki} &= \int_{\Gamma_t} N_K^u n_j \sigma_{ij}'' d\Gamma \\
(f_4^u)_{Ki} &= \int_{\Gamma_p} N_K^u (\alpha - n) n_i p d\Gamma \\
(f_5^u)_{Ki} &= \int_{\Omega} N_K^u (1-n) \rho_s b_i d\Omega \\
(f_1)_{Ki} &= \int_{\Gamma_p} n N_K^U n_i p d\Gamma \\
(f_2)_{Ki} &= \int_{\Omega} N_K^U \rho_f b_i d\Omega
\end{aligned} \tag{3.17}$$

$\mathbf{N}^u, \mathbf{N}^p, \mathbf{N}^U$ are shape functions of the skeleton fluid and pore pressure. The expressions ρ, ρ_s, ρ_f are the density of the total, and the solid and fluid phases, respectively. The porosity n , is used in the definition $\rho = (1-n)\rho_s + n\rho_f$.

3.3 Fully Coupled Analysis of Soils in Large Deformation Realm

Development of the finite element formulation for solving fully coupled, solid-fluid problems in geomechanics has also begin. The formulation is based on earlier work of [Biot, 1972]; [Zienkiewicz and Shiomi, 1984]; [Coussy, 1995]; and [Jeremić et al., 2001].

The formulation is quite general in that it can handle elastic-plastic geomaterials subjected to arbitrarily large deformations. The formulation is also capable of treating compressible and/or incompressible pore fluid. The Lagrangian format is assumed for the solid phase while deformations of the fluid phase are written in Eulerian format. It is shown that the multiplicative decomposition of the deformation gradient, utilized in the large deformation elastic-plastic formulation for solid phase, can be used to precisely control the volumetric response of the fluid phase. The fluid content is decomposed additively. The basic unknown variables are the absolute displacement of solid phase (u_i), pore pressure (p), and relative displacement of fluid phase (U_i). The strong form is based on the Equation of Motion (3.18), Fluid Mass Conduction (3.19), and Fluid Mass Conservation (3.20).

$$P_{ij,j} + (r_o + m)b_i - \rho_o^s(1 - n)\ddot{u}_i - (m + \rho_o^{fl} n)\ddot{U}_i = 0 \quad (3.18)$$

$$JnF_{ij}^{-1}\dot{U}_i + k_{ij} \left[p_{,j} + \rho^{fl} F_{ij} b_i - \rho^{fl} F_{ij} \ddot{U}_i - \rho^{fl} F_{ij} a_i \right] = 0 \quad (3.19)$$

$$(1 - n)\dot{E}_{ii}\rho^{fl} + \left(\frac{n}{K_{fl}} + \frac{(1 - n)}{K_s} \right) (\dot{p} + p_{,i}u_i) + J\rho^{fl}n \left(F_{ij}^{-1}\dot{U}_{i,j} + F_{i,j}^{-1}\dot{U}_i \right) = 0 \quad (3.20)$$

where the following notation is used: P_{ij} = First Piola–Kirchhoff stress tensor; r_o = Mass density; m = Fluid mass content per initial volume; b_i = Body force; ρ_o^s = Initial mass density for solid phase; ρ_o^{fl} = Initial mass density for fluid phase; n = Porosity; F_{ij} = deformation Gradient; J = Jacobian of the transformation $J = \det F_{ij}$; k_{ij} = Permeability tensor (anisotropic); ρ^{fl} = Current mass density for fluid phase; a_i = Tortuosity vector; D_{km} = Lagrange strain rate; E_{IJ} = Lagrange strain tensor; K_s = Bulk modulus of the solid phase; and K_{fl} = Bulk modulus of the fluid phase.

The development of this formulation is nearing completion and implementation in OpenSees will start soon.

Chapter 4

Visualization

Our work on visualization is guided by the need to understand the vast output of 3D simulations of soil–foundation–structure interactions. The work is progressing on two fronts. The first is a collaboration with the Center for Image Processing and Interactive Computing (CIPIC) at UC Davis on visualizing tensor fields in 3D, more specifically visualizing stress tensor fields using a program named **Fantom** [Scheuermann et al., 2000]. This work has already resulted in a submitted paper [Jeremić et al., 2001]. The second front involves performing less fancy visualizations of models (meshes), plastic zones, and various other results from simulations using the **Joey3D** graphics program, specifically developed for the visualization of OpenSees outputs from solid elements.

This chapter presents examples of both tensor visualizations as well as visualizations using **Joey3D**.

4.1 Visualizations Using Fantom

Figures 4.1(a,b) shows hyperstreams-surfaces for minor principal stress (compression) for (a) a single-pile and (b) a four-pile group example. In Figure 4.1(a), the hyperstreams-surface starts at the center line of a pile and extends through the concrete (in both directions) until it reaches the surrounding soil. The hyperstreams-surface shown in Figure 4.1(a) reveals the stress field in more detail. The twisting and “discoloring” of the hyperstreams-surface toward the bottom of the pile can be explained by the fact that the stress field in the

concrete pile is far away from the main bending effects close to the surface. The state of stress thus deviates by just a small amount from the initial state induced by its own weight. Such a small change in stresses leads to a near-uniform green hue. A “kink” in direction and color noticeable close to the surface is a part of the hyperstreamsurface that ends in the soil, and thus by moving from a stiff (concrete) toward a soft (soil) medium, has much smaller minor (compressive) stresses.

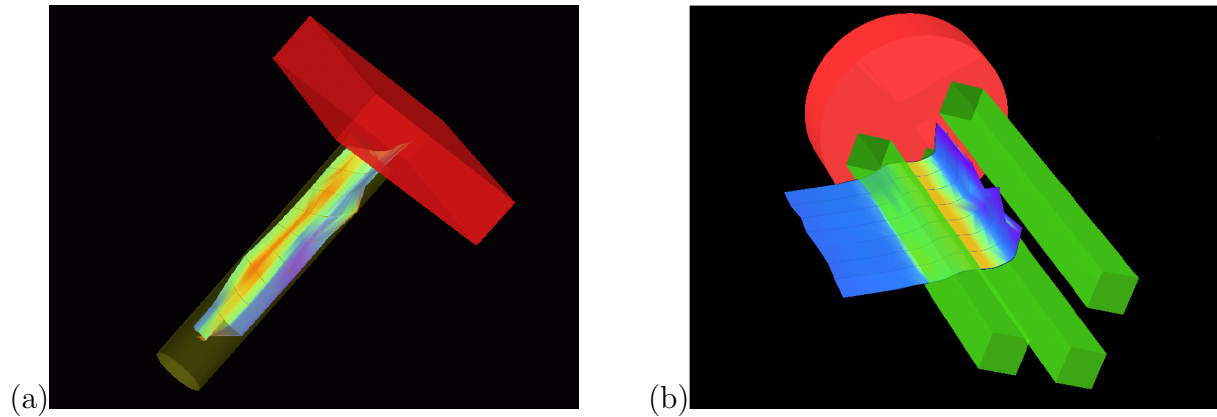


Figure 4.1: Hyperstreamsurfaces for minor principal stress (compression) for (a) a single-pile and (b) a four-pile group.

Figure 4.1(b) represents the minor (compressive) principal stress hyperstreamsurface for the four-pile group. In this figure one pile was removed from the model to simplify the view. Note the interesting “shading” effect apparent behind the left pile in this figure. The hyperstreamsurface starts at the center of that pile and extends outside, ending in soil. This pile group is much stiffer than the one-pile example. The effects of bending are much smaller, and the four-pile group behaves like a stiff frame embedded in soil. The observed deformation pattern is thus closer to horizontal translation with a large horizontal resistance and small bending. The hyperstreamsurface extends into the soil outside the pile group, with apparent compressive stress. However, just behind the pile but inside the pile group, the minor principal stress changes significantly in value and then curves by almost 90° . The twist of the minor principal stress hyperstreamsurface clearly demonstrates the pile-group effect: Maximal compressive stress (minor principal stress) is acting between two piles in a direction perpendicular to the pile loading direction. This

finding contradicts the current belief about stresses in pile groups. More important, a large “shading” effect is observed which, when combined with the twisting of the minor principal stress, suggests that the two back piles are loaded mostly in a direction perpendicular to the global loading direction.

4.2 Visualization Using Joey3D

While developments related to the Phantom program deal more with new methods for visualization of the results of geomechanics computations, the necessities of visualizing day-to-day results have led us to develop a simple graphics program based on the OpenGL graphics libraries. The program is named Joey3D and some illustrative visualizations obtained by using this program are presented below.

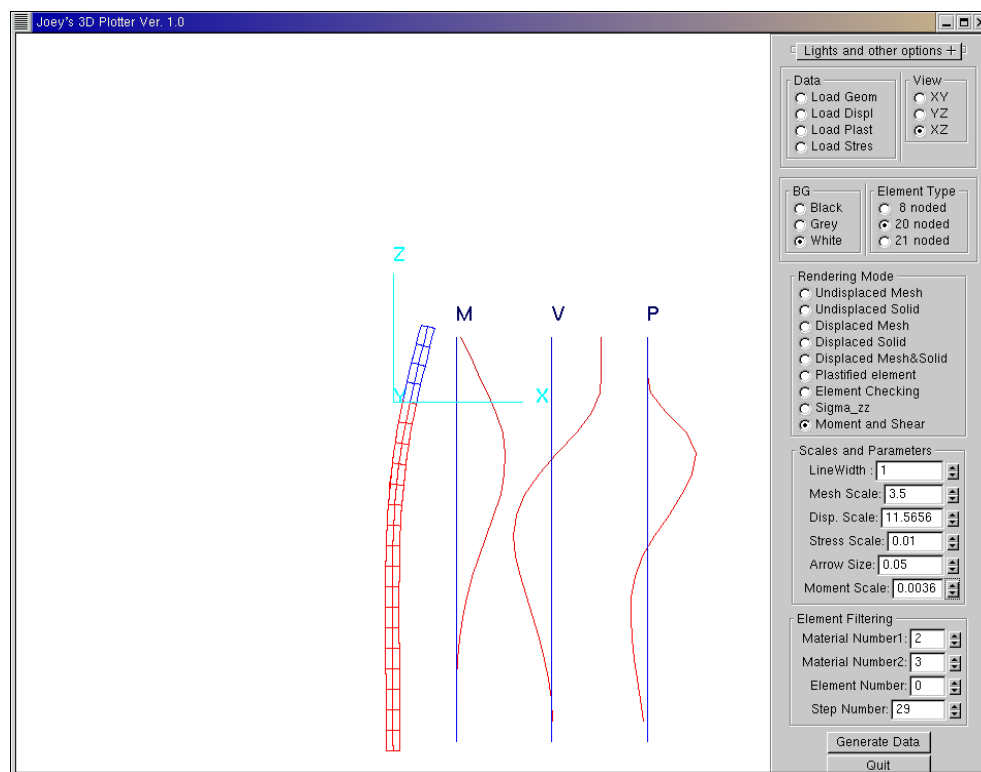


Figure 4.2: Visualization with Joey3D: displaced piles, moment diagram (from integrated normal stresses), shear force diagram (from integrated shear stresses), and horizontal pressure (from the first derivatives of shear forces).

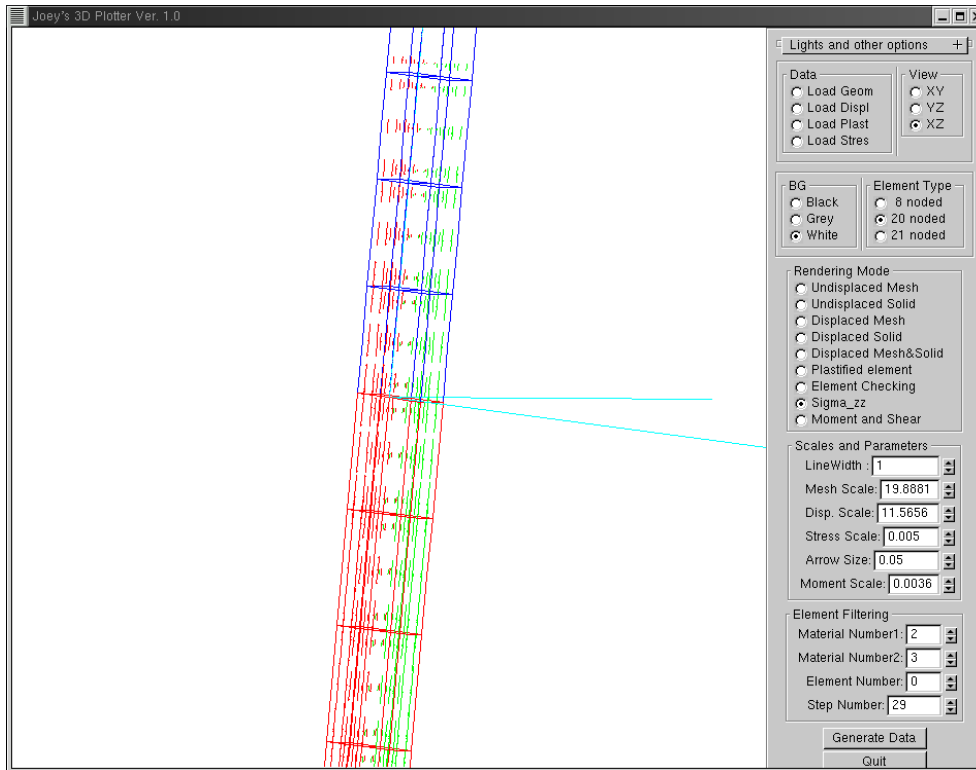


Figure 4.3: Visualization with Joey3D: normal stresses in a solid pile.

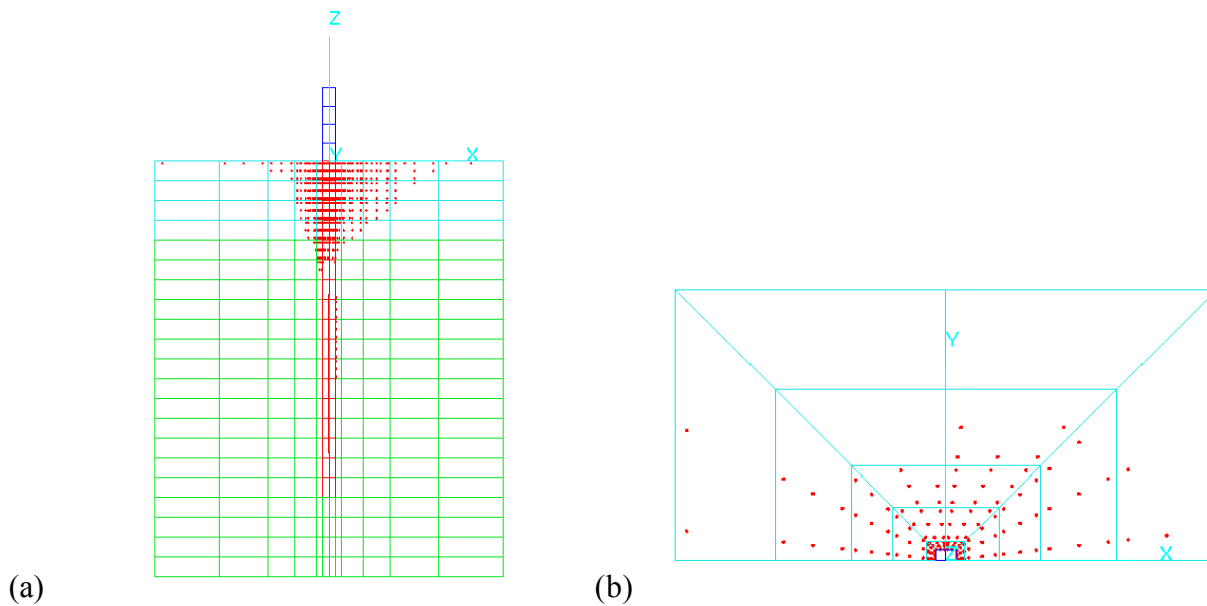


Figure 4.4: Plastified zones (plastic Gauss-points) during static pushover analysis of single pile. Visualization with Joey3D: (a) side view, (b) top (plan) view.

Chapter 5

Examples of

Soil–Foundation–Structure

Interaction Simulations

The research described also included performing a number of SFS interaction simulations to test the concepts presented in previous chapters. Both static and dynamic simulations were performed. Some illustrative examples are presented below. More detailed analysis results can be found at web–site:

<http://sokocalo.engr.ucdavis.edu/~jeremic/OpenSees/Piles>.

5.1 Static Pushover Tests

A number of static pushover tests were simulated for a single pile. In the analysis currently being done the behavior of a single pile system in layered soils is being analyzed. Figure 5.1 shows the model and the finite element mesh.

Figures 5.2 and 5.3 show plastic zones (plastified Gauss–points) for the two cases. Case #1 comprises layers of sand and clay; case #2 comprises a single layer of clay throughout the soil.

Also developed was the automatic generation of P–Y curves from numerical simulation results. Some initial results are presented in Figures 5.4 and 5.5.

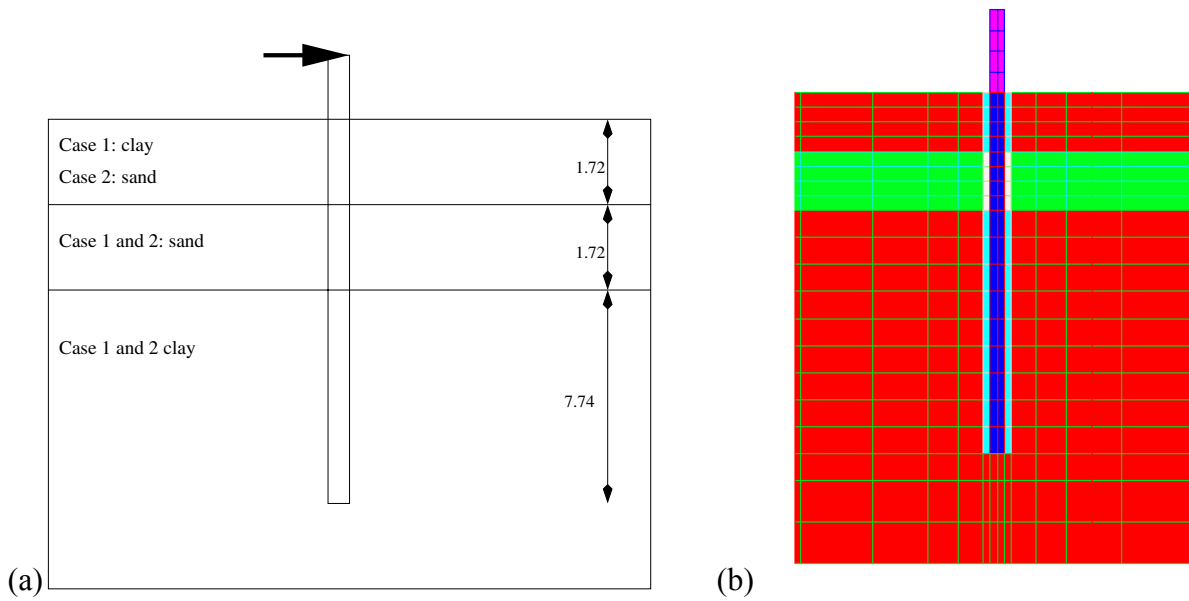


Figure 5.1: (a) Single pile model, dimensions and layers of sand and clay. (b) Single pile model, side view; top four finite elements are clay, middle four layers of finite elements are sand and the bottom is all clay; interface zone around the concrete pile is also present.

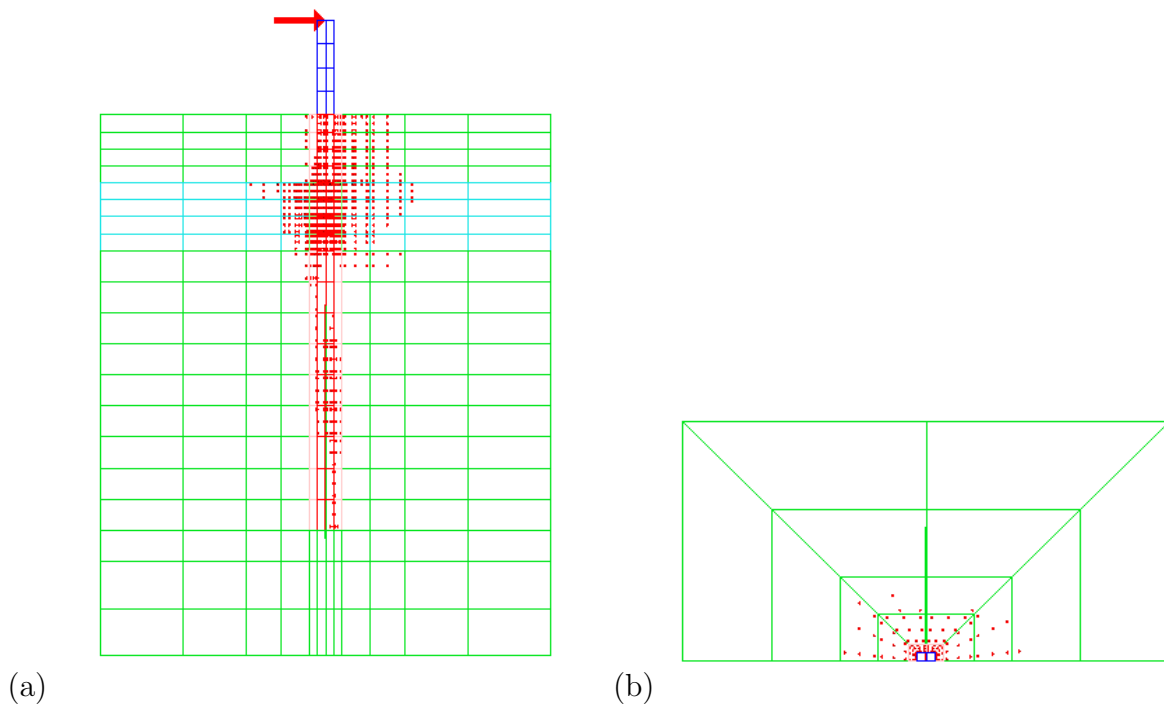


Figure 5.2: Plastic zone at the end of loading for case 1, layers of sand and clay: (a) side view, (b) top view.

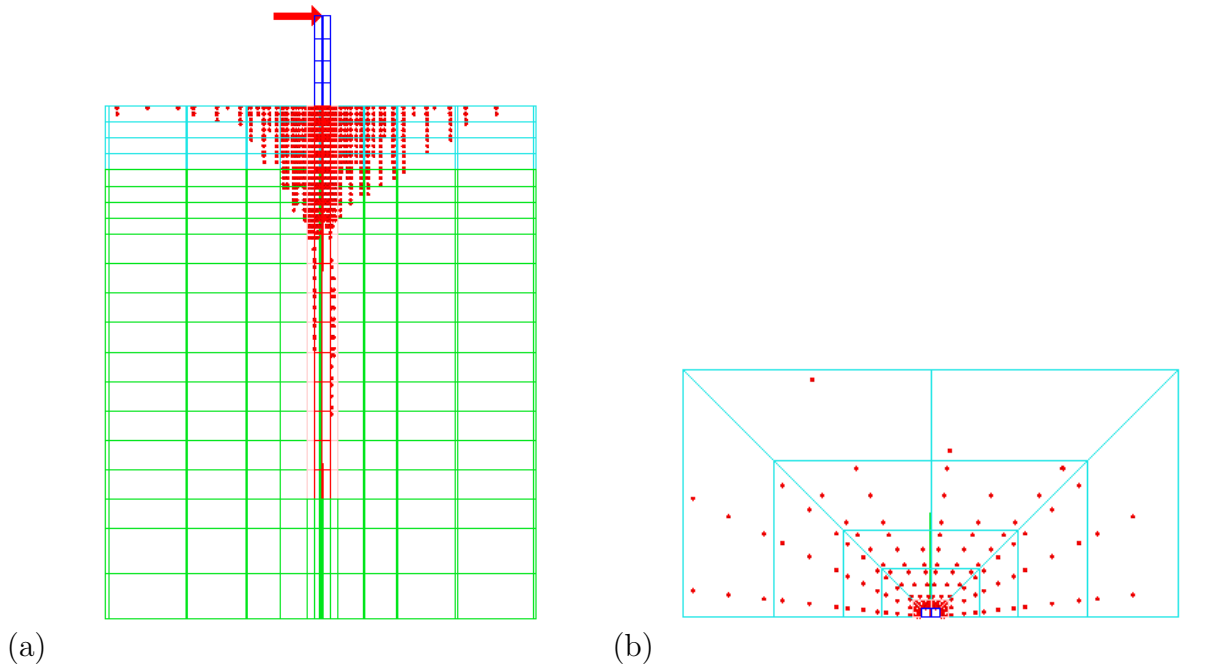


Figure 5.3: Plastic zone at the end of loading for case 2, single layer of clay: (a) side view, (b) top view.

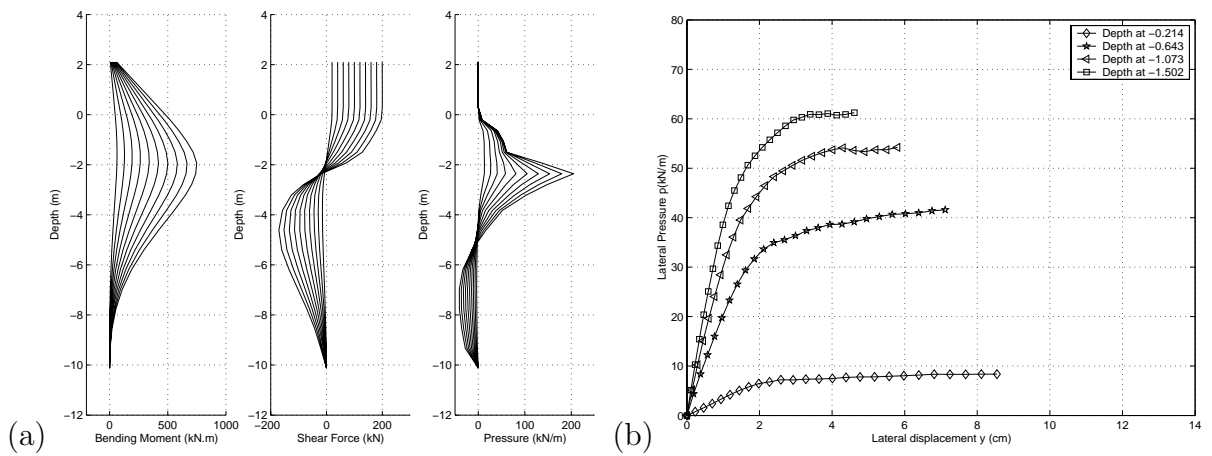


Figure 5.4: (a) Moment, shear force, and pressure distribution (clay-sand profile); (b) p-y curves (clay-sand profile).

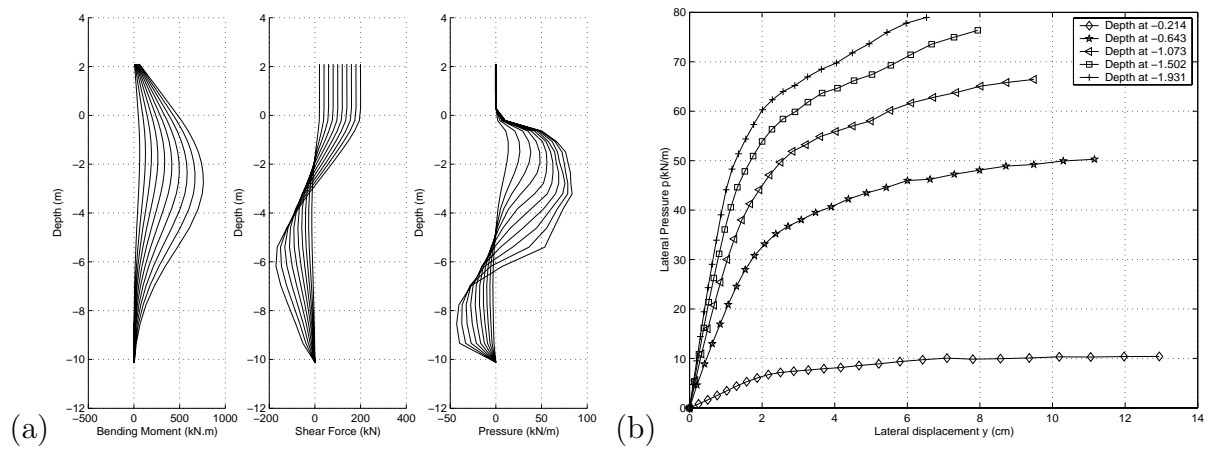


Figure 5.5: (a) Moment, shear force, and pressure distribution (clay profile); (b) p-y curves (clay profile).

5.2 Humboldt Bay Bridge Retrofit

The Humboldt Bay Bridge simulations comprise before and after retrofit analysis of one of the foundation systems during a synthetic earthquake, provided by Dr. Abbas Abghari of Caltrans.

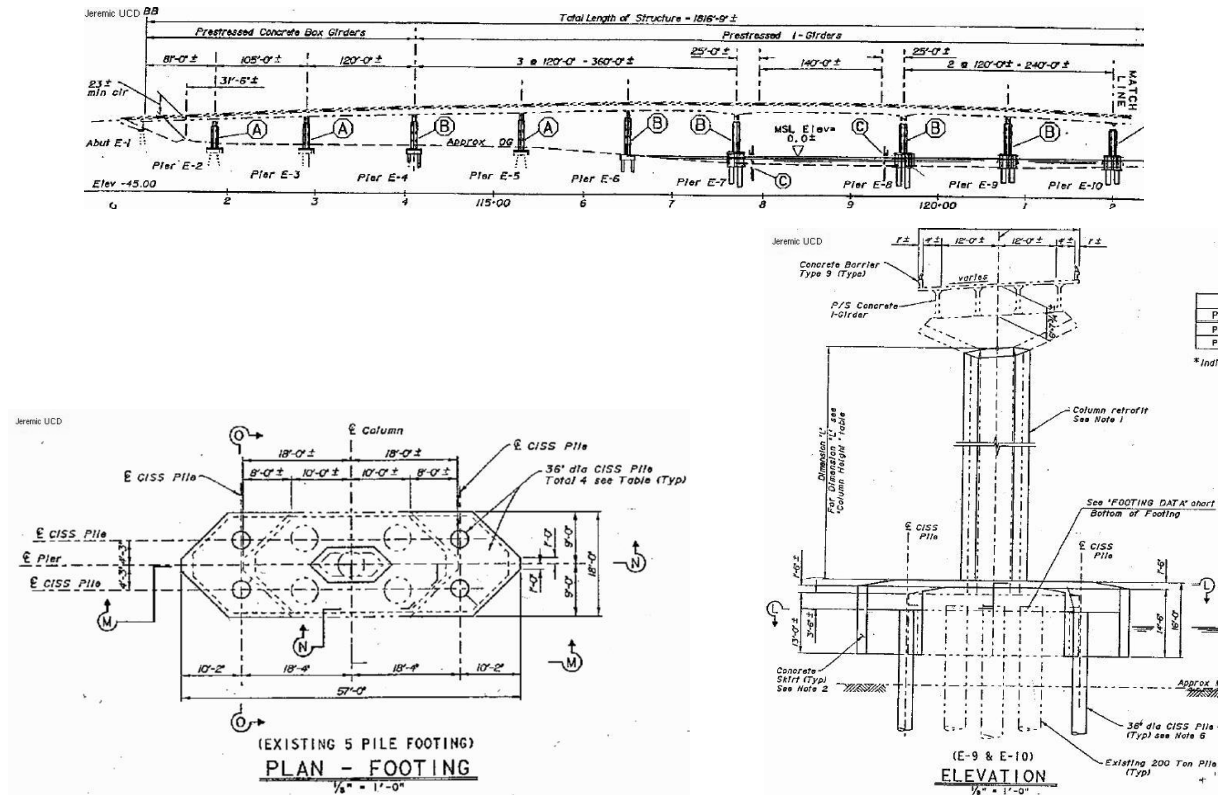


Figure 5.6: Humboldt Bay Bridge plan of the SFS system.

The material models used for soil are a version of rotational kinematic hardening Drucker–Prager (for dense sand). The initial friction angle was at 37° . Figure 5.9 shows a selected response (displacements and accelerations) for before and after the retrofit models. This simulation was not intended to give definite answers on the actual retrofit, so an in-depth study of the differences was not performed. The goal was to show that OpenSees can indeed perform such simulations.

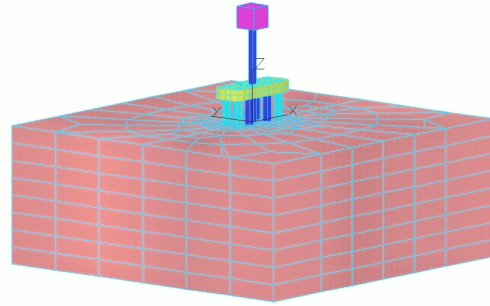
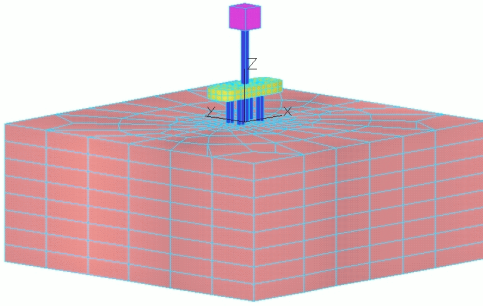


Figure 5.7: Humboldt Bay Bridge: before and after the retrofit finite element models.

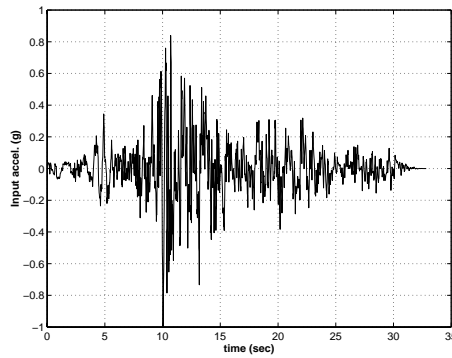


Figure 5.8: Synthetic accelerations used in this analysis.

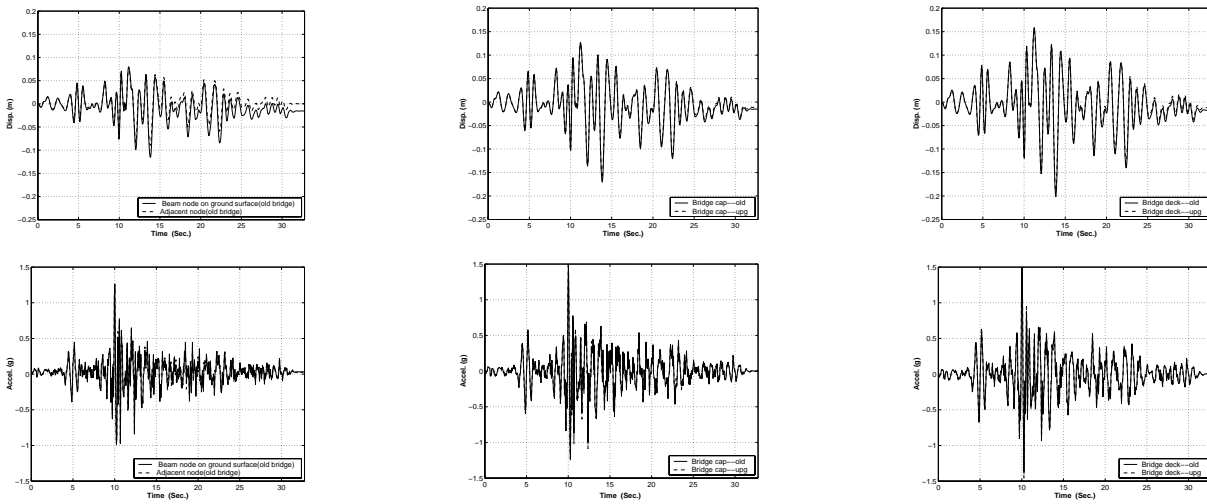


Figure 5.9: Response for the before and after the retrofit SFS system.

Chapter 6

Implementation Quality Control

One of the often neglected components of software development is the quality control of the actual implementation. Beyond making sure that the models implemented do perform as expected, one has to be confident that the implementation is free of bugs and follows certain minimum standards. In order to test the quality of implementation for the OpenSees finite element platform, a number of automatic tests have been implemented that can be performed on a request, by developers, for example, or on a regular basis. To this end, The following programming tools were used to test the implementation quality:

- Codewizard from Parasoft Inc.
- Insure from Parasoft Inc.
- g++ from GNU
- KCC from Kuck and Associates, Inc.
- pgCC from Portland Group Inc.

The Codewizard tool is used to perform C++ standard compliance tests. The Insure tool is used to track various bugs and memory leaks. The set of compilers (g++, KCC, and pgCC are used to clear most of the warnings and errors reported. This cross-compiler testing ensures that the code is as close to the standard as possible and is portable.

Recent implementation quality control reports are available at <http://sokocalo.engr.ucdavis.edu/~jeremic/OpenSees/BugReports>.

Bibliography

- [Biot, 1972] Biot, M. A. (1972). Theory of finite deformations of porous solids. *Indiana University Mathematical Journal*, 21(7):597–620.
- [Coussy, 1995] Coussy, O. (1995). *Mechanics of Porous Continua*. John Wiley and Sons. ISBN 471 95267 2.
- [Jeremić et al., 2001] Jeremić, B., Runesson, K., and Sture, S. (2001). Finite deformation analysis of geomaterials. *International Journal for Numerical and Analytical Methods in Geomechanics including International Journal for Mechanics of Cohesive–Frictional Materials*, 25(8):809–840.
- [Jeremić et al., 2001] Jeremić, B., Scheuermann, G., Frey, J., Yang, Z., Hamann, B., Joy, K. I., and Hagen, H. (2001). Tensor visualizations in computational geomechanics. *International Journal for Numerical and Analytical Methods in Geomechanics*. Accepted for publication, October 2001. available as CGM report: <http://sokocalo.engr.ucdavis.edu/~jeremic/publications/CGM0101.pdf>.
- [Jeremić and Sture, 1998] Jeremić, B., and Sture, S. (1998). Tensor data objects in finite element programming. *International Journal for Numerical Methods in Engineering*, 41:113–126.
- [Jeremić and Yang, 2001] Jeremić, B., and Yang, Z. (2001). Template elastic–plastic computations in geomechanics. *International Journal for Numerical and Analytical Methods in Geomechanics*. Accepted for publications, available as CGM report at: <http://sokocalo.engr.ucdavis.edu/~jeremic/publications/CGM0102.pdf>.

- [Manzari and Dafalias, 1997] Manzari, M. T., and Dafalias, Y. F. (1997). A critical state two-surface plasticity model for sands. *Géotechnique*, 47(2):255–272.
- [Ousterhout and Tcl/Tk Consortium,] Ousterhout, J., and Tcl/Tk Consortium. Tool command language (Tcl), tool kit (Tk) gui. <http://www.tclconsortium.org/> and <http://www.scriptics.com/>
- [Scheuermann et al., 2000] Scheuermann, G., Frey, J., and Bobach, T. (2000). Field analysis using topology methods (fantom) visualization program. <http://daddi.informatik.uni-kl.de>.
- [Zienkiewicz and Shiomi, 1984] Zienkiewicz, O. C., and Shiomi, T. (1984). Dynamic behaviour of saturated porous media; the generalized Biot formulation and it's numerical solution. *International Journal for Numerical Methods in Engineering*, 8:71–96.